

# Quantum oscillation in Hopf-link semimetals

Lei Shi<sup>†,1,2</sup> Xiaoxiong Liu<sup>†,1,2</sup> C. M. Wang,<sup>3</sup> Tianyu Liu,<sup>4,5</sup> Hai-Zhou Lu,<sup>1,2,\*</sup> and X. C. Xie<sup>6,7,8</sup>

<sup>1</sup>Department of Physics and Guangdong Basic Research Center of Excellence for Quantum Science, Southern University of Science and Technology (SUSTech), Shenzhen 518055, China

<sup>2</sup>Quantum Science Center of Guangdong-Hong Kong-Macao Greater Bay Area (Guangdong), Shenzhen 518045, China

<sup>3</sup>Department of Physics, Shanghai Normal University, Shanghai 200234, China

<sup>4</sup>International Quantum Academy, Shenzhen 518048, China

<sup>5</sup>Shenzhen Key Laboratory of Quantum Science and Engineering, Shenzhen 518055, China

<sup>6</sup>International Center for Quantum Materials, School of Physics, Peking University, Beijing 100871, China

<sup>7</sup>Institute for Nanoelectronic Devices and Quantum Computing, Fudan University, Shanghai 200433, China

<sup>8</sup>Hefei National Laboratory, Hefei 230088, China

(Dated: December 11, 2024)

Since the discovery of the relation between the Chern number and quantum Hall effect, searching for observables of topological invariants has been an intriguing topic. Topological Hopf-link semimetals have attracted tremendous interest, in which the conduction and valence energy bands touch at linked nodal lines. However, it is challenging to identify this sophisticated topology. We propose to use the quantum oscillation in strong magnetic fields to probe the Hopf links. For a generic model of Hopf-link semimetal that captures the linked-trivial phase transition, we figure out the phase shifts of oscillation for all Fermi pockets in all magnetic-field directions, by presenting self-consistent results from the Fermi surface tomography, Landau fan diagram, and electrical resistivity. As the magnetic field is rotated, the phase shifts exhibit a unique pattern, which could help to identify Hopf links in real materials, such as those in  $\text{Li}_2\text{NaN}$ .

**Introduction** - Observables associated with topological invariants is an intriguing topic. The well-known paradigms include the Chern number for the quantum Hall effects [1–5],  $\mathbb{Z}_2$  invariant for the quantum spin Hall effect [6], winding number for the Su-Shrieffer-Heeger model of polyacetylene [7, 8], Euler characteristic for ballistic conductor [9, 10], Hopf invariant that maps 3D spheres to 2D [11–14], skyrmion number for magnetic vortices [15, 16]. Recently, an emerging Hopf-link semimetal has attracted great attention [17–21], in which the conduction and valence energy bands touch at linked nodal lines or nodal rings (Fig. 1). The Hopf links have been realized mainly in bosonic systems, such as photonic crystals [22], superconducting circuits [23], trapped ion simulator [24], topological Raman lattice [25, 26]. However, in real materials, due to lack of practical probes and clear signatures, the Hopf link has only been observed in  $\text{Co}_2\text{MnGa}$  by using angle-resolved photoemission spectroscopy [27].

In this Letter, we propose that the Hopf links could be probed by the quantum oscillation of resistance, which arises from the Landau quantization of electronic states under strong magnetic fields. The oscillation can be described by  $\cos[2\pi(F/B + \Phi)]$ , where  $B$  is the strength of magnetic field and the oscillation frequency  $F$  and phase shift  $\Phi$  can provide valuable Fermi-surface and topological properties of energy bands [28, 29]. We systematically study the phase shifts of quantum oscillation in all magnetic-field directions for a generic model that describes a linked-trivial transition of a nodal ring and a nodal line, with the help of three self-consistent approaches, including the Fermi-surface tomography, resistivity, and Landau fan diagrams. For the Hopf-link

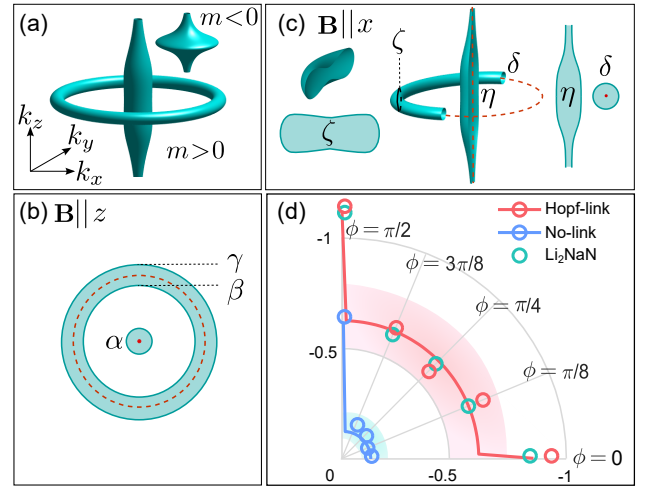


FIG. 1. (a) Fermi surfaces of a Hopf-link semimetal ( $m > 0$ ) and the trivial case ( $m < 0$ ).  $m$  is a model parameter in Eq. (2).  $k_x, k_y, k_z$  are the wave vectors. [(b) and (c)] Extremal cross sections of the Hopf-link semimetal in a magnetic field  $\mathbf{B}$  along the  $z$  and  $x$  directions, respectively. The red dashed lines indicate the linked nodal ring and nodal line where the conduction and valence energy bands touch. (d) As the magnetic field is rotated from  $\phi = 0$  through  $\pi/2$ , the extremal cross sections transit from  $(\alpha, \beta, \gamma)$  to  $(\eta, \delta, \zeta)$ , and the summation of phase shifts from all cross sections (solid lines from analytical and circles from numerical results) form a unique pattern for the Hopf-link semimetal and  $\text{Li}_2\text{NaN}$  (red shadow), compared to the trivial case (blue shadow).

semimetal, we can always identify three distinct phase shifts, which evolve as the magnetic field is rotated, forming a unique pattern [Fig. 1(d)] that may facilitate identifying Hopf links in realistic materials, such as  $\text{Li}_2\text{NaN}$  (Fig. 3).

### Phase shifts extracted from Fermi-surface tomography.

– Figure 1(a) shows the Fermi surface of a generic Hopf-link semimetal ( $m > 0$ ), where the conduction and valence energy bands touch at some points of momentum (i.e., the nodes). The nodes form a nodal ring and a nodal line linked with each other. In a strong magnetic field, the Lorentz force forces electrons to perform the cyclotron motion, creating a confinement that quantizes the energy bands into a series of 1D bands of Landau levels (e.g., see Fig. 2(a)). As the bands cross the Fermi energy one by one, the resistance or conductance may show a series of peaks, that is, the Shubnikov de Haas quantum oscillation. The quantum oscillation is characterized by its frequency  $F$  and phase shift  $\Phi$ . The frequency  $F = (\hbar/2\pi e)A$  is determined by the Fermi-surface extremal cross-sectional area  $A$  perpendicular to the magnetic field, i.e., the Onsager relation [30], where  $\hbar$  is the reduced Planck constant and  $e$  is the elementary charge. In conventional metals, the phase shift  $\Phi$  is believed to follow the rules [28, 29]

$$\Phi = -1/2 + \Phi_B/2\pi + \Phi_{3D}, \quad (1)$$

where  $\Phi_B$  is the Berry phase [31], which is  $\pi$  around a nodal line [32] due to the one-to-one correspondence between the momentum-dependent winding number and wavefunction of the drumhead surface states [33].  $\Phi_{3D} = \pm 1/8$  is a correction that occurs only in three dimensions. For a maximal (minimal) cross section,  $\Phi_{3D} = -1/8$  ( $1/8$ ) for electron carriers and  $\Phi_{3D} = 1/8$  ( $-1/8$ ) for hole carriers.

However, the conventional rules have never been tested for the topological bands as sophisticated as those of Hopf-link semimetals. Therefore, we compare the phase shifts from the rules with those from a direct calculation of resistance, trying to give a signature of the Hopf link in the quantum oscillation measurement. Figure 1(b) shows the extremal cross sections  $\alpha$ ,  $\beta$ , and  $\gamma$  in a magnetic field normal to the nodal-ring plane ( $\mathbf{B} \parallel \mathbf{z}$ ). The three cross sections correspond to three oscillation frequencies, each has a phase shift. Throughout the work, we restrict our discussion for electron carriers. The outer maximal ( $\gamma$ ) and inner minimal ( $\beta$ ) cross sections along the nodal ring have no Berry phase, so their phase shifts are supposed to be  $-1/2 + 0 - 1/8 = -5/8$  and  $-1/2 + 0 + 1/8 = -3/8$ . The  $\alpha$  minimal cross-section encloses the nodal line, thus has a  $\pi$  Berry phase and a phase shift of  $-1/2 + \pi/2\pi + 1/8 = 1/8$ . Figure 1(c) shows the  $\delta$ ,  $\zeta$ , and  $\eta$  extremal cross sections in a magnetic field parallel to the nodal-ring plane ( $\mathbf{B} \parallel \mathbf{x}$ ). The minimal cross-section  $\delta$  around the nodal ring has a  $\pi$  Berry phase, so its phase shift is  $-1/2 + \pi/2\pi + 1/8 = 1/8$ . The other two maximal cross sections  $\eta$  and  $\zeta$  have no Berry phase in the first Brillouin zone, resulting in the same phase shift  $-1/2 + 0 - 1/8 = -5/8$  for two different frequencies. The phase shifts in other directions of magnetic field can be argued similarly, as summarized

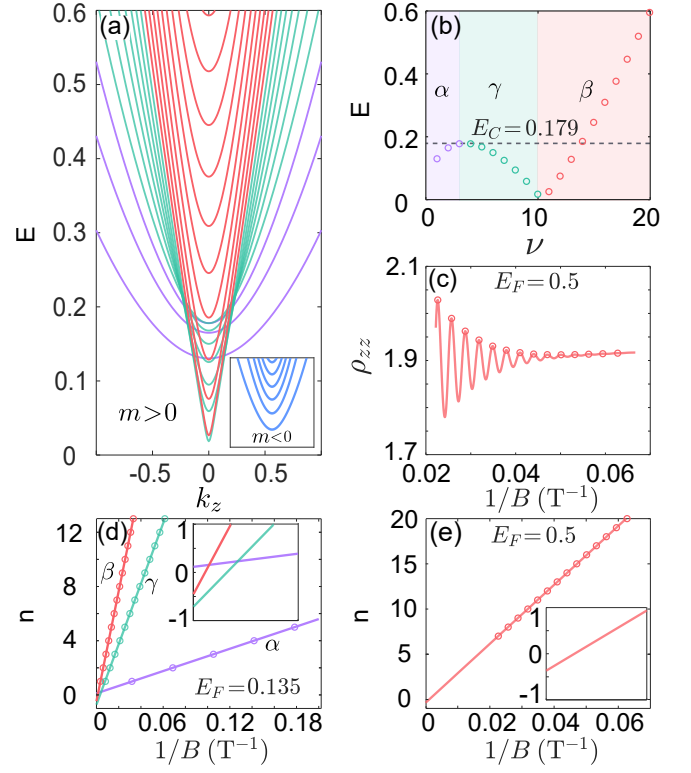


FIG. 2. Landau bands under a 30T  $z$ -direction magnetic field. (a) Energies of the Landau bands for the Hopf-link semimetal ( $m = 0.5$ ) as functions of the wave vector  $k_z$ . The purple, red, and green bands correspond to the  $\alpha$ ,  $\beta$ , and  $\gamma$  cross sections in Fig. 1(b), respectively. Inset: Landau bands for the trivial case ( $m = -1$ ). (b) The dependence of the band-bottom ( $k_z = 0$ ) energies on the Landau index  $\nu$  distinguishes the  $\alpha$ ,  $\beta$ , and  $\gamma$  Landau bands. Above a critical energy  $E_C = 0.179$  (dashed line), only the  $\beta$  bands contribute to band bottoms. (c) At the Fermi energy  $E_F = 0.5 > E_C$ , the  $z$ -direction resistivity  $\rho_{zz}$  as a function of  $1/B$  contributed from the  $\beta$  bands, where  $B$  is the strength of the  $z$ -direction magnetic field. (d) The band index  $n$  of the resistivity peaks from all bands as a function of  $1/B$  at  $E_F = 0.135$ . Inset: Zoom-in of the intersects on the  $n$  axis, which give the phase shifts listed in the  $\phi = 0$  rows and Numeric  $\Phi$  column in Tab. I. (e) The band index  $n$  of the resistivity peaks from  $\beta$  bands as a function of  $1/B$  at  $E_F = 0.5$ . Inset: Zoom-in of the intersect on the  $n$  axis.

in the Analytic  $\Phi$  column of Tab. I. In contrast, the inset of Fig. 1(a) shows that the trivial case ( $m < 0$ ) has only one Fermi surface. It has an only maximal cross section, regardless of the magnetic field's orientation. It has a  $\pi$  Berry phase and a phase shift of  $-1/2 + \pi/2\pi - 1/8 = -1/8$  in the  $z$ -direction magnetic field, and no Berry phase and a phase shift of  $-1/2 + 0 - 1/8 = -5/8$  in the  $x$ -direction magnetic field. The phase shifts of the only cross section in other directions of magnetic field are also summarized in the Analytic  $\Phi$  column of Tab. I.

Interestingly, Fig. 1(d) shows that, the summation of

the phase shifts of all cross sections as a function of the angle of magnetic field  $\phi$  form a unique pattern for the linked case (red shadow), in sharp contrast to the trivial case (blue shadow). This pattern can be understood as a poor man's conservation law of the phase shifts as the extremal cross sections transit with the direction of magnetic field. More importantly, the quantum oscillation measurement is readily accessible [34–48], so this pattern could serve as a signature to identify the Hopf link.

**Phase shifts extracted from resistivity.** – To verify the above results, we need to calculate the resistivity. We start with a generic Hamiltonian of Hopf-link semimetal

$$\mathcal{H}(\mathbf{k}) = [k_x k_z + (m - Ck^2) k_y] \hat{\sigma}_x + [-k_y k_z + (m - Ck^2) k_x] \hat{\sigma}_y, \quad (2)$$

where  $k^2 = k_x^2 + k_y^2 + k_z^2$ ,  $k_x, k_y, k_z$  are the wave vectors,  $C = 0.5$ ,  $\hat{\sigma}_x$  and  $\hat{\sigma}_y$  are the Pauli matrices [18]. When  $m > 0$ , this model hosts a nodal line at  $k_x = k_y = 0$ , as well as a nodal ring at  $k_x^2 + k_y^2 = 2m$  on the  $k_z = 0$  plane, forming a Hopf link, as shown in Fig. 1(a). When  $m < 0$ , the model is trivial with no Hopf link, as shown in the inset of Fig. 1(a). We consider a magnetic field  $\mathbf{B} = B(\sin \phi, 0, \cos \phi)$  that rotates in the  $x$ - $z$  plane, with the strength of magnetic field  $B$  and the angle of magnetic field  $\phi \equiv \arctan(B_x/B_z)$ . We solve the 1D energy bands of Landau levels as functions of the wave vector  $k_{\parallel} = k_x \sin \phi + k_z \cos \phi$  along the direction of magnetic field, which remains invariant under the Lorentz force. When the magnetic field is along the  $z$  direction ( $\phi = 0$ ), for the Landau index  $\nu \geq 1$ , the eigen energies of the Landau bands can be solved analytically as

$$E_{k_{\parallel}}^{\nu \pm} = \pm \sqrt{\nu[M_{\parallel}^2 + (\cos \phi + 1)^2 M_{\nu}^2]} / (\sqrt{2} \ell_B), \quad (3)$$

where magnetic length  $\ell_B \equiv \sqrt{1/eB}$ ,  $M_{\parallel} = k_{\parallel}(\cos 2\phi + \cos \phi)$ ,  $M_{\nu} = m - k_{\parallel}^2/2 - (\nu + 1/2)\omega_c$ , and oscillation frequency  $\omega_c \equiv 2C/\ell_B^2$ . But  $E_{k_{\parallel}}^0 = 0$  for  $\nu = 0$ . The Planck constant  $\hbar$  is set to 1 in this toy model. Figure 2(a) shows the Landau bands of the Hopf-link semimetal ( $m = 0.5$ ) when the magnetic field is along the  $z$  direction. The bands consist of three sets (except the zero-energy  $\nu = 0$  band), as shown by the purple, red, and green bands, corresponding to the  $\alpha$ ,  $\beta$ , and  $\gamma$  cross sections in Fig. 1(b), respectively. The energies of the  $\alpha$  and  $\beta$  bands from the minimal cross sections shift upward with increasing  $\nu$ . By contrast, those of the  $\gamma$  bands from the maximal cross section shift downward with increasing  $\nu$ , as shown in terms of their band-bottom energies in Fig. 2(b). The inset of Fig. 2(a) shows the Landau bands for the trivial case ( $m = -1$ ), which consists of only one set, because there is only one maximal cross section, consistent with the inset of Fig. 1(a).

To capture the phase shift, we calculate the resistivity  $\rho_{zz} = 1/\sigma_{zz}$  along the  $z$  direction of the Landau bands

TABLE I. Phase shift  $\Phi$  of the maximal (Max) or minimal (Min) cross sections for the electron Fermi pockets in Fig. 1, obtained by using Eq. (1) (Analytic) and numerically calculated from the resistivity  $\rho_{zz}$  or from the Landau fan diagram of band-bottom energies (Numeric). The angle of magnetic field is defined as  $\phi \equiv \arctan(B_x/B_z)$ .  $\kappa$  is the maximal cross section of the trivial case.

$\phi$	Cross section	Berry phase	Analytic $\Phi$	Numeric $\Phi$
0	$\alpha$ (Min)	$\pi$	1/8	0.115 $\pm$ 0.016
	$\beta$ (Min)	0	-3/8	-0.366 $\pm$ 0.011 ( $\rho_{zz}$ )
	$\gamma$ (Max)	0	-5/8	-0.390 $\pm$ 0.007
	$\kappa$ (Max)	$\pi$	-1/8	-0.684 $\pm$ 0.003
$\pi/8$	$\kappa$ (Max)	$\pi$	-1/8	-0.141 $\pm$ 0.009 ( $\rho_{zz}$ )
	$\eta$ (Max)	$\pi$	-1/8	-0.121 $\pm$ 0.028
	$\delta$ (Min)	$\pi$	1/8	-0.129 $\pm$ 0.000
	$\zeta$ (Max)	0	-5/8	0.114 $\pm$ 0.001
$\pi/4$	$\kappa$ (Max)	$\pi$	-1/8	-0.680 $\pm$ 0.000
	$\eta$ (Max)	$\pi$	-1/8	-0.126 $\pm$ 0.000
	$\delta$ (Min)	$\pi$	1/8	-0.145 $\pm$ 0.022
	$\zeta$ (Max)	0	-5/8	0.146 $\pm$ 0.015
$3\pi/8$	$\kappa$ (Max)	$\pi$	-1/8	-0.561 $\pm$ 0.007
	$\eta$ (Max)	$\pi$	-1/8	-0.149 $\pm$ 0.001
	$\delta$ (Min)	$\pi$	1/8	-0.159 $\pm$ 0.000
	$\zeta$ (Max)	0	-5/8	0.099 $\pm$ 0.002
$\pi/2$	$\kappa$ (Max)	$\pi$	-1/8	-0.584 $\pm$ 0.008
	$\eta$ (Max)	0	-5/8	-0.168 $\pm$ 0.000
	$\delta$ (Min)	$\pi$	1/8	-0.650 $\pm$ 0.000
	$\zeta$ (Max)	0	-5/8	0.127 $\pm$ 0.000
$\pi$	$\kappa$ (Max)	0	-5/8	-0.624 $\pm$ 0.026
	$\zeta$ (Max)	0	-5/8	-0.677 $\pm$ 0.000

(details in Sec. SIII of [49]), with the conductivity

$$\sigma_{zz} = \frac{e^2}{2\pi\ell_B^2} \sum_{n \in \nu, \pm} \int \frac{dk_z}{2\pi} \tau_{k_x, k_z}^n (v_z^{n, k_z})^2 \delta(E_{k_z}^n - E_F). \quad (4)$$

The  $z$ -direction velocity of band  $n$  at  $k_z$  for degenerate states is calculated by  $v_z^{n, k_z} = \partial E_{k_z}^n / \partial k_z$ , and  $\tau_{k_x, k_z}^n$  is the scattering time of band  $n$  at  $k_z$  with the degenerate Landau levels denoted by  $k_x$ . When the Fermi level  $E_F$  is set to 0.5, only the  $\beta$  band bottoms can cross the Fermi energy, as shown in Fig. 2(b). The corresponding  $\rho_{zz}$  as a function of  $1/B$  with a series of peaks is shown in Fig. 2(c). The phase shift can be captured by searching the intersect of the band index  $n$  as a function of  $1/B$  at the peak positions. We yield  $\Phi = -0.366 \pm 0.011$  for the  $\beta$  cross section at  $\phi = 0$ , which consistent with  $-3\pi/8$  in Tab. I. For the trivial case, the phase shift extracted from  $\rho_{zz}$  is  $-0.141 \pm 0.009$  (Fig. S1 of [49]), close to  $-\pi/8$  in Tab. I for the  $\kappa$  cross section at  $\phi = 0$ .

**Phase shifts extracted from Landau fan diagram of band-bottom energies** – The above results infer that the

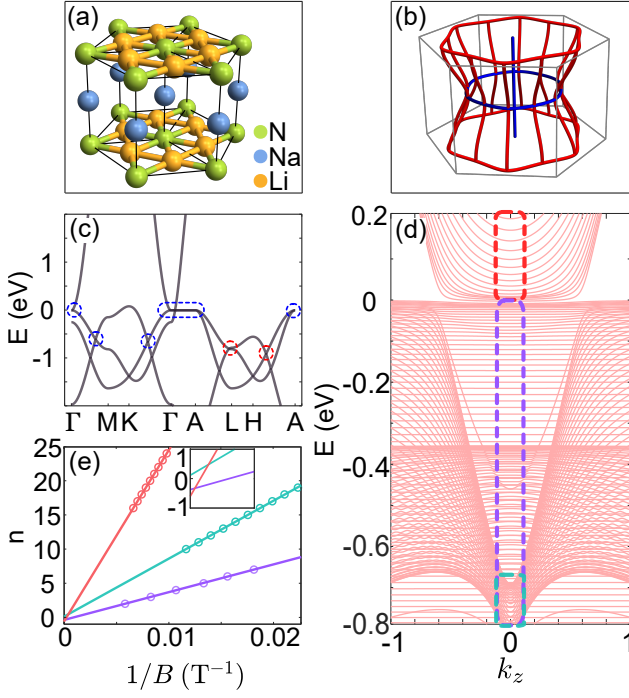


FIG. 3. The predicted Hopf-link semimetal material Li<sub>2</sub>NaN [50]. (a) Crystal structure of Li<sub>2</sub>NaN. (b) Nodal lines of Li<sub>2</sub>NaN in the first Brillouin zone, including a Hopf link (blue) consisting of a nodal-line and a nodal-ring, and additional nodal lines (red). (c) Band structure described by the tight-binding model in Eq. (5) on high-symmetry lines, where Fermi energy is 0 eV. The blue dashed rings indicates the nodal-lines (at Fermi energy) and nodal-rings (-0.6 eV below Fermi energy) of the blue Hopf-link. The red dashed rings indicate the red additional nodal lines. (d) The Landau-band energies under  $B_z = 10$  T as functions of the wave vector  $k_z$ . (e) The  $n-1/B$  plots for three distinct frequencies, extracted from the band-bottom energies (indicated by the dashed boxes at  $k_z = 0$  in (d)) at the Fermi energy  $E_F = -0.75$  (green),  $-0.2$  (purple), and  $0.75$  eV (red), respectively. The intercepts on the  $n$  axis (Inset: Zoom-in) give the phase shifts, as listed in Tab. II at  $\phi = 0$ .

resistivity peaks correspond to the bottoms of the Landau bands. Specifically, the  $n-1/B$  relation is found at those values of  $B$  when the bottom of the  $n$ -th band crosses the Fermi energy, i.e., Landau Fan diagram. In Fig. 2 (c), there is only one frequency from the  $\beta$  cross section, because the Fermi energy  $E_F$  is higher than the critical value  $E_C$ . When  $E_F < E_C$ , Fig. 2 (d) shows three  $n-1/B$  plots with different slopes, corresponding to all three cross sections in Fig. 1 (b). The phase shifts extracted from Fig. 2 (d) are listed in the Numeric column in Tab. I at  $\phi = 0$ , which are consistent with those in the Analytic column. It can further justifying the effectiveness of our approach method to capture the phase shifts. Therefore, we generalize the approach to arbitrary directions of magnetic field by numerically calculating the Landau bands (details in Sec. SIV of [49]), as shown by

the Numeric column in Tab. I, for  $\phi = \pi/8, \pi/4, 3\pi/8$ , and  $\pi/2$ , where  $\phi = \pi/2$  corresponds to  $\mathbf{B} \parallel x$ .

**Realistic material Li<sub>2</sub>NaN** - Now we apply the above approach to a realistic material Li<sub>2</sub>NaN [50]. The energy spectrum near the Fermi energy of Li<sub>2</sub>NaN can be described by a four-band tight-binding model

$$\mathcal{H}_{\text{eff}} = \sum_{i\alpha} \varepsilon_{\alpha} c_{i\alpha}^{\dagger} c_{i\alpha} + \sum_{i\alpha, j\beta} t_{\alpha, \beta}^{i, j} c_{i\alpha}^{\dagger} c_{j\beta}, \quad (5)$$

where  $c_{i\alpha}^{\dagger}$  ( $c_{i\alpha}$ ) are electron creation (annihilation) operators on the  $\alpha$  orbital at lattice site  $i$ ,  $\varepsilon_{\alpha}$  is the on-site energy of the  $\alpha$  orbital, and  $t_{\alpha, \beta}^{i, j}$  is the hopping integral between the  $\alpha$  orbital on site  $i$  and  $\beta$  orbital on site  $j$  (detailed expressions in Sec. SV of [49]). The Hopf link described by this model is shown by the blue part in Fig. 3(b). The red part in Fig. 3(b) represents some additional nodal lines well separated from the nodal line of the Hopf-link in both momentum and energy. Their effects can be excluded by choosing proper chemical potentials when analyzing the phase shifts.

TABLE II. Numerically calculated phase shifts from Landau fan diagrams for Li<sub>2</sub>NaN. The angle of magnetic field is defined as  $\phi \equiv \arctan(B_x/B_z)$ . The  $\alpha, \beta, \gamma, \eta, \delta$  and  $\zeta$  indicate the corresponding cross sections in Tab. I.

$\phi$	Phase shift $\Phi$		
0	$0.115 \pm 0.000$ ( $\alpha$ )	$-0.372 \pm 0.016$ ( $\beta$ )	$-0.601 \pm 0.001$ ( $\gamma$ )
$\pi/8$	$-0.119 \pm 0.004$ ( $\eta$ )	$0.111 \pm 0.006$ ( $\delta$ )	$-0.616 \pm 0.029$ ( $\zeta$ )
$\pi/4$	$-0.164 \pm 0.000$ ( $\eta$ )	$0.153 \pm 0.001$ ( $\delta$ )	$-0.595 \pm 0.001$ ( $\zeta$ )
$3\pi/8$	$-0.180 \pm 0.000$ ( $\eta$ )	$0.161 \pm 0.009$ ( $\delta$ )	$-0.587 \pm 0.000$ ( $\zeta$ )
$\pi/2$	$-0.571 \pm 0.000$ ( $\eta$ )	$0.118 \pm 0.002$ ( $\delta$ )	$-0.624 \pm 0.053$ ( $\zeta$ )

By applying the magnetic field  $\mathbf{B} = B(\sin \phi, 0, \cos \phi)$  to the tight-binding model, the hopping integrals become carrying the flux of magnetic field in terms of a path integral  $t_{\alpha, \beta}^{i, j} \rightarrow t_{\alpha, \beta}^{i, j} \exp[i(2\pi/\phi_0) \int_{R_j}^{R_i} d\ell \cdot \mathbf{A}]$ , where the flux quantum  $\phi_0 = h/e$  and  $\mathbf{A}$  is the vector potential of the magnetic field (Sec. SV of [49]). The Landau bands of Li<sub>2</sub>NaN, as shown in Fig. 3(c) is calculated by diagonalize the effective tight-binding model under a  $z$ -direction magnetic field. The Landau bands also can be identified by three sets. We use the band-bottom energies [dashed boxes in Fig. 3(d)] to plot the  $n-1/B$  relation in Fig. 3(e), to extract the three phase shifts  $0.115, -0.372$ , and  $-0.601$ , respectively, as listed in Tab. II at  $\phi = 0$ . The results are consistent with the phase shifts found from the generic model in Tab. I for the Analytic and Numeric columns at  $\phi = 0$ . The phase shifts in other directions of magnetic field can be found similarly (Sec. SV of [49]), as shown in Tab. II for  $\phi = \pi/8, \pi/4, 3\pi/8$ , and  $\pi/2$ , which are also consistent with those from the generic model in Tab. I. More importantly, the phase shifts of Li<sub>2</sub>NaN also form a similar pattern as that of the generic model, as compared by the green and red circles in Fig. 1(d).



**Acknowledgments** – <sup>†</sup>Lei Shi and Xiaoxiong Liu contribute equally. This work was supported by the National Key R&D Program of China (2022YFA1403700), Innovation Program for Quantum Science and Technology (2021ZD0302400), the National Natural Science Foundation of China (11534001, 12350402, 11974249, and 11925402), Guangdong Basic and Applied Basic Research Foundation (2023B0303000011), Guangdong province (2020KCXTD001), Guangdong Provincial Quantum Science Strategic Initiative (GDZX2201001 and GDZX2401001), the Science, Technology and Innovation Commission of Shenzhen Municipality (ZDSYS20190902092905285), and Center for Computational Science and Engineering of SUSTech.

---

\* Corresponding author: [luhz@sustech.edu.cn](mailto:luhz@sustech.edu.cn)

- [1] K. v. Klitzing, G. Dorda, and M. Pepper, New method for high-accuracy determination of the fine-structure constant based on quantized hall resistance, *Phys. Rev. Lett.* **45**, 494 (1980).
- [2] D. J. Thouless, M. Kohmoto, M. P. Nightingale, and M. den Nijs, Quantized Hall conductance in a two-dimensional periodic potential, *Phys. Rev. Lett.* **49**, 405 (1982).
- [3] H. Z. Lu, W. Y. Shan, W. Yao, Q. Niu, and S. Q. Shen, Massive Dirac fermions and spin physics in an ultrathin film of topological insulator, *Phys. Rev. B* **81**, 115407 (2010).
- [4] R. Yu, W. Zhang, H.-J. Zhang, S.-C. Zhang, X. Dai, and Z. Fang, Quantized anomalous Hall effect in magnetic topological insulators, *Science* **329**, 61 (2010).
- [5] C.-Z. Chang, J. Zhang, X. Feng, J. Shen, Z. Zhang, M. Guo, K. Li, Y. Ou, P. Wei, L.-L. Wang, *et al.*, Experimental observation of the quantum anomalous Hall effect in a magnetic topological insulator, *Science* **340**, 167 (2013).
- [6] C. L. Kane and E. J. Mele, Quantum spin Hall effect in graphene, *Phys. Rev. Lett.* **95**, 226801 (2005).
- [7] I. Mondragon-Shem, T. L. Hughes, J. Song, and E. Prodan, Topological criticality in the chiral-symmetric AIII class at strong disorder, *Phys. Rev. Lett.* **113**, 046802 (2014).
- [8] J. Song and E. Prodan, AIII and BDI topological systems at strong disorder, *Phys. Rev. B* **89**, 224203 (2014).
- [9] C. L. Kane, Quantized nonlinear conductance in ballistic metals, *Phys. Rev. Lett.* **128**, 076801 (2022).
- [10] P. M. Tam and C. L. Kane, Probing fermi sea topology by Andreev state transport, *Phys. Rev. Lett.* **130**, 096301 (2023).
- [11] J. E. Moore, Y. Ran, and X.-G. Wen, Topological surface states in three-dimensional magnetic insulators, *Phys. Rev. Lett.* **101**, 186805 (2008).
- [12] D.-L. Deng, S.-T. Wang, C. Shen, and L.-M. Duan, Hopf insulators and their topologically protected surface states, *Phys. Rev. B* **88**, 201105 (2013).
- [13] C. Liu, F. Vafa, and C. Xu, Symmetry-protected topological Hopf insulator and its generalizations, *Phys. Rev. B* **95**, 161116 (2017).
- [14] Z.-Y. Zhuang and Z. Yan, Extrinsic and intrinsic non-linear Hall effects across Berry-dipole transitions, *Phys. Rev. B* **107**, L161102 (2023).
- [15] M. Onoda, G. Tatara, and N. Nagaosa, Anomalous Hall effect and skyrmion number in real and momentum spaces, *J. Phys. Soc. Jpn.* **73**, 2624 (2004).
- [16] N. Nagaosa and Y. Tokura, Topological properties and dynamics of magnetic skyrmions, *Nat. Nanotechnol.* **8**, 899 (2013).
- [17] W. Chen, H.-Z. Lu, and J.-M. Hou, Topological semimetals with a double-helix nodal link, *Phys. Rev. B* **96**, 041102(R) (2017).
- [18] Z. Yan, R. Bi, H. Shen, L. Lu, S.-C. Zhang, and Z. Wang, Nodal-link semimetals, *Phys. Rev. B* **96**, 041103(R) (2017).
- [19] M. Ezawa, Topological semimetals carrying arbitrary Hopf numbers: Fermi surface topologies of a Hopf link, Solomon's knot, trefoil knot, and other linked nodal varieties, *Phys. Rev. B* **96**, 041202(R) (2017).
- [20] C. Zhong, Y. Chen, Z.-M. Yu, Y. Xie, H. Wang, S. A. Yang, and S. Zhang, Three-dimensional pentagon carbon with a genesis of emergent fermions, *Nat. Commun.* **8**, 15641 (2017).
- [21] Y. Zhou, F. Xiong, X. Wan, and J. An, Hopf-link topological nodal-loop semimetals, *Phys. Rev. B* **97**, 155140 (2018).
- [22] G.-G. Liu, Z. Gao, Q. Wang, X. Xi, Y.-H. Hu, M. Wang, C. Liu, X. Lin, L. Deng, S. A. Yang, *et al.*, Topological Chern vectors in three-dimensional photonic crystals, *Nature* **609**, 925 (2022).
- [23] X. Tan, M. Li, D. Li, K. Dai, H. Yu, and Y. Yu, Demonstration of Hopf-link semimetal bands with superconducting circuits, *Appl. Phys. Lett.* **112**, 172601 (2018).
- [24] M.-M. Cao, K. Li, W.-D. Zhao, W.-X. Guo, B.-X. Qi, X.-Y. Chang, Z.-C. Zhou, Y. Xu, and L.-M. Duan, Probing complex-energy topology via non-hermitian absorption spectroscopy in a trapped ion simulator, *Phys. Rev. Lett.* **130**, 163001 (2023).
- [25] J. Yu, Measuring Hopf links and Hopf invariants in a quenched topological Raman lattice, *Phys. Rev. A* **99**, 043619 (2019).
- [26] C.-R. Yi, J.-L. Yu, W. Sun, X.-T. Xu, S. Chen, and J.-W. Pan, Observation of the Hopf links and Hopf fibration in a 2D topological Raman lattice (2019), [arXiv:1904.11656](https://arxiv.org/abs/1904.11656).
- [27] I. Belopolski, G. Chang, T. A. Cochran, Z.-J. Cheng, X. P. Yang, C. Hugelmeier, K. Manna, J.-X. Yin, G. Cheng, D. Multer, *et al.*, Observation of a linked-loop quantum state in a topological magnet, *Nature* **604**, 647 (2022).
- [28] I. Lifshitz and A. Kosevich, Theory of magnetic susceptibility in metals at low temperatures, *Sov. Phys. JETP* **2**, 636 (1956).
- [29] D. Shoenberg, *Magnetic oscillations in metals* (Cambridge University Press, 1984).
- [30] L. Onsager, Interpretation of the de Haas-van Alphen effect, *Philos. Mag. Ser. 1* **43**, 1006 (1952).
- [31] D. Xiao, M.-C. Chang, and Q. Niu, Berry phase effects on electronic properties, *Rev. Mod. Phys.* **82**, 1959 (2010).
- [32] G. P. Mikitik and Y. V. Sharlai, Manifestation of berry's phase in metal physics, *Phys. Rev. Lett.* **82**, 2147 (1999).
- [33] G.-Q. Zhao, S. Li, W. B. Rui, C. M. Wang, H.-Z. Lu, and X. C. Xie, 3d quantum Hall effect in a topological nodal-ring semimetal, *Quant. Front.* **2**, 22 (2023).
- [34] H. Murakawa, M. S. Bahrany, M. Tokunaga, Y. Ko-

- hama, C. Bell, Y. Kaneko, N. Nagaosa, H. Y. Hwang, and Y. Tokura, Detection of Berry's phase in a bulk Rashba semiconductor, [Science](#) **342**, 1490 (2013).
- [35] C. M. Wang, H.-Z. Lu, and S.-Q. Shen, Anomalous phase shift of quantum oscillations in 3D topological semimetals, [Phys. Rev. Lett.](#) **117**, 077201 (2016).
- [36] C. Li, C. M. Wang, B. Wan, X. Wan, H.-Z. Lu, and X. C. Xie, Rules for phase shifts of quantum oscillations in topological nodal-line semimetals, [Phys. Rev. Lett.](#) **120**, 146602 (2018).
- [37] L. P. He, X. C. Hong, J. K. Dong, J. Pan, Z. Zhang, J. Zhang, and S. Y. Li, Quantum transport evidence for the three-dimensional Dirac semimetal phase in  $\text{Cd}_3\text{As}_2$ , [Phys. Rev. Lett.](#) **113**, 246402 (2014).
- [38] M. Novak, S. Sasaki, K. Segawa, and Y. Ando, Large linear magnetoresistance in the Dirac semimetal  $\text{TlBiSe}_2$ , [Phys. Rev. B](#) **91**, 041203 (2015).
- [39] Y. Zhao, H. Liu, C. Zhang, H. Wang, J. Wang, Z. Lin, Y. Xing, H. Lu, J. Liu, Y. Wang, *et al.*, Anisotropic fermi surface and quantum limit transport in high mobility three-dimensional Dirac semimetal  $\text{Cd}_3\text{As}_2$ , [Phys. Rev. X](#) **5**, 031037 (2015).
- [40] R. Singha, A. K. Pariari, B. Satpati, and P. Mandal, Large nonsaturating magnetoresistance and signature of nondegenerate Dirac nodes in  $\text{ZrSiS}$ , [Proc. Natl. Acad. Sci. U.S.A.](#) **114**, 2468 (2017).
- [41] M. N. Ali, L. M. Schoop, C. Garg, J. M. Lippmann, E. Lara, B. Lotsch, and S. S. P. Parkin, Butterfly magnetoresistance, quasi-2D Dirac Fermi surface and topological phase transition in  $\text{ZrSiS}$ , [Sci. Adv.](#) **2**, e1601742 (2016).
- [42] X. Wang, X. Pan, M. Gao, J. Yu, J. Jiang, J. Zhang, H. Zuo, M. Zhang, Z. Wei, W. Niu, *et al.*, Evidence of both surface and bulk Dirac bands and anisotropic non-saturating magnetoresistance in  $\text{ZrSiS}$ , [Adv. Electron. Mater.](#) **2**, 1600228 (2016).
- [43] Y.-Y. Lv, B.-B. Zhang, X. Li, S.-H. Yao, Y. B. Chen, J. Zhou, S.-T. Zhang, M.-H. Lu, and Y.-F. Chen, Extremely large and significantly anisotropic magnetoresistance in  $\text{ZrSiS}$  single crystals, [Appl. Phys. Lett.](#) **108**, 244101 (2016).
- [44] J. Hu, Y. L. Zhu, D. Graf, Z. J. Tang, J. Y. Liu, and Z. Q. Mao, Quantum oscillation studies of the topological semimetal candidate  $\text{zrgem}$  ( $m = s, se, te$ ), [Phys. Rev. B](#) **95**, 205134 (2017).
- [45] H. Pan, B. Tong, J. Yu, J. Wang, D. Fu, S. Zhang, B. Wu, X. Wan, C. Zhang, X. Wang, *et al.*, Three-dimensional anisotropic magnetoresistance in the Dirac node-line material  $\text{ZrSiSe}$ , [Sci. Rep.](#) **8**, 9340 (2018).
- [46] J. Hu, Z. Tang, J. Liu, X. Liu, Y. Zhu, D. Graf, K. Myhro, S. Tran, C. N. Lau, J. Wei, *et al.*, Evidence of topological nodal-line fermions in  $\text{ZrSiSe}$  and  $\text{ZrSiTe}$ , [Phys. Rev. Lett.](#) **117**, 016602 (2016).
- [47] J. Hu, Z. Tang, J. Liu, Y. Zhu, J. Wei, and Z. Mao, Nearly massless Dirac fermions and strong Zeeman splitting in the nodal-line semimetal  $\text{ZrSiS}$  probed by de Haas-van Alphen quantum oscillations, [Phys. Rev. B](#) **96**, 045127 (2017).
- [48] N. Kumar, K. Manna, Y. Qi, S.-C. Wu, L. Wang, B. Yan, C. Felser, and C. Shekhar, Unusual magnetotransport from Si-square nets in topological semimetal  $\text{HfSiS}$ , [Phys. Rev. B](#) **95**, 121109 (2017).
- [49] Supplemental Material.
- [50] P. M. Lenggenhager, X. Liu, S. S. Tsirkin, T. Neupert, and T. c. v. Bzdušek, From triple-point materials to multiband nodal links, [Phys. Rev. B](#) **103**, L121101 (2021).